Grain-Boundaries-Engineering via Laser Manufactured La-Doped BaSnO₃ Nanocrystals with Tailored Surface States Enabling Perovskite Solar Cells with Efficiency of 23.74%

Xiaokun Yang [a, b], Wenhao Zhao[a], Mingjie Li[a], Linfeng Ye [a], Pengfei Guo [a], Youxun Xu [a], Hang Guo[a], Qian Ye [a], Hongyue Wang [a], Daniel Harvey [c], Huiwu Yu [a], Minjun Feng[b], Tze-Chien Sum[b], Dmitry Shchukin* [c], Hongqiang Wang* [a]

[a]State Key Laboratory of Solidification Processing, Center for Nano Energy Materials, School of Materials Science and Engineering, Northwestern Polytechnical University and Shaanxi Joint Laboratory of Graphene (NPU), Xi'an, 710072, P. R. China

Email: hongqiang.wang@nwpu.edu.cn

[b]School of Physical & Mathematical Sciences, Nanyang Technological University, 21 Nanyang Link, Singapore 637371

[c]Stephenson Institute for Renewable Energy, Department of Chemistry, University of Liverpool, Crown Street, Liverpool, L69 7ZD, UK

Email: d.shchukin@liverpool.ac.uk

Abstract: Grain boundaries (GBs) engineering of hybrid perovskite films is of significance for accessing high performance perovskite solar cells (PSCs), owing to the abundant defect states existed therein originating from the low temperature film processing. Nanocrystals embedding at GBs has shown profound advantages in carrier dynamics modulation, while the surface defects on nanocrystals in turn lead usually to the trapping of carriers at GBs. The authors herein demonstrate the efficient GBs engineering via laser generated nanocrystals with tailored surface states for improved carriers dynamics and environmental stability of PSCs. The embedding of La doped BaSnO₃ (LBSO) nanocrystals with bare surfaces in perovskite provides an additional channel to facilitate the effective carrier extraction and reduce the carrier recombination, leading to a maximum power conversion efficiency (PCE) of 21.11% with negligible hysteresis for the mixed-cation PSCs. To clarify the influence of surface defect states of the laser generated nanocrystals on the performance of PSCs, 1H,1H-perfluorooctylamine is grafted on LBSO nanocrystals during the laser irradiation, resulting in improved champion PCE up to 21.65% and pronounced environmental stability. The universal embedding of the LBSO nanocrystals with tailored surface states in different perovskite by fabricating FAPbI₃ PSCs with a champion PCE of 23.74% is further demonstrated.

1. Introduction

During last decade, perovskite solar cells (PSCs) have been under intensive investigation owing to their unique optoelectric properties such as long carrier's diffusion length[1], strong optical absorptivity[2], ambipolar charge transport[3], tunable optical band gap[4], as well as the solution processability, which leads to the rapid increase of power conversion efficiency (PCE) from an unstable 3.8%[5] to confirmed 25.2%[6]. Such progress in PSCs performance is mainly benefited from adjustment in perovskite components[7-9], solvent engineering[10-11], additives introduction[12-14] and device configuration optimization[15-18]. Among the reported solvent engineering, the anti-solvent based strategy has been widely adopted to obtain the flat and homogeneous pinhole-free film. Since the first report by Seok et al. that adopted toluene as anti-solvent [11], various anti-solvents such as chlorobenzene[19], diethyl ether (ether)[20], ethyl acetate (EA)[21] and even mixed anti-solvent[22-23] have been explored to grow high quality perovskite films. In addition, the anti-solvent strategy allows for the possibility of introducing different additives that could interact with perovskite matrix. Preliminary successes have been demonstrated by dissolving small molecules or polymers in anti-solvent to control the film morphology and passivate the defects located at either interface or grain boundaries (GBs), leading to effectively improved photovoltaic performance[24-27]. Worth noting that the additives of the passivation molecules or polymers could cause barriers of charge transfer owing to their intrinsic lower carrier mobility/conductivity comparing to that of the hybrid perovskite matrix[28-30], even this can be balanced by their passivation effects. Solid additives with intrinsic higher carrier mobility are thus preferable for the decoration of perovskite films for enhanced photovoltaic performance, but have been rarely reported. The main reason could be due to the challenge of dispersing desired nanosized solid additives that could remain in the perovskite film after the high-speed spin coating in the anti-solvent procedure.

Ternary oxide semiconductors have been widely investigated for a vast range of applications[31] (e.g., dielectrics, sensors, photocatalysts, and solar cells), as their chemical properties and band structure can easily be modified by altering the composition and doping, which have been chosen as electron transport layer in perovskite solar cells community[18, 32]. Inspired by the success of constructing heterojunction in perovskite films to accelerate the extraction and transport of photogenerated electrons by dissolving and dispersing solid additives (such as $A_{10}C_{60}$ fullerene derivative[33], PCBM[34] and Graphdiyne (GDY)[35]) with high carrier mobility and appropriate band structure in precursor, embedding ternary oxide

semiconductors in the bulk film may be a promising strategy for improving its bulk charge transport. It would thus be attractive and promising if a strategy is developed for introducing the solid additives of ternary metal oxides with high carrier mobility in the perovskite film via the typical anti-solvent method, which is anticipated to provide a platform to investigate the interaction between the solid additive and perovskite matrix for modulated optoelectric performance. We demonstrate herein the generation of the nanocrystals of La-doped $BaSnO_3$ (LBSO), an n-type semiconductor material that has high electron mobility of 320 cm^2 V^{-1} S^{-1} [36], by using a technique of pulsed laser irradiation in liquid. Owing to the advances of such technology in yielding nanocrystals in desired solvent, the LBSO nanocrystals dispersed in the anti-solvent of ethyl acetate were successfully embedded in the surfaces and grain boundaries of the perovskite film. We found such embedding had no influence on the film morphology and crystallinity while great impact on the optical and electric properties on the film matrix, which led to hysteresis-negligible triple cation planar PSCs with a champion efficiency up to 21.11%. The achievement of such enhanced performance was verified to be due to the effective carrier extraction and suppressed recombination process brought by the embedding of the LBSO nanocrystals in the perovskite films.

2. Results and Discussion

LBSO nanocrystals generated by pulsed laser irradiation in liquid

LBSO raw nanoparticles are synthesized by following previously reported methods in the literature [18] and the preparation details are given in the methods. **Figure 1a** shows the scanning electron microscopy (SEM) image of raw LBSO nanoparticles, where the nanoparticles are strongly agglomerated. A histogram plotted by analyzing more than 150 particles is shown in the inset, indicating that raw LBSO nanoparticles have an average size of 40 nm. The corresponding X-ray diffraction (XRD) pattern shows that the phase transformation in the two-step reaction (**Figure 1b)** and the eventually synthesized raw LBSO nanoparticles have the identical cubic crystal phase with BSO (PDF card number: 01-089-2488), indicating that La atom do not induce conspicuous structural change in the cubic BSO due to similar atomic size, shown in **Figure 1c**. We further confirm the doping of La via characterizations of X-ray photoelectron spectroscopy (XPS) for LBSO powders, as shown in **Figure 1c**, and the two characteristic spin-orbit peaks of La $3d_{5/2}$ and $3d_{3/2}$ are detected (detailed XPS information of LBSO shown in **Figure S1**).

Figure 1d depicts the typical process where LBSO colloidal solution can be generated by pulsed laser irradiation of raw LBSO nanoparticles in the anti-solvent of EA. In brief, 1 mg of raw LBSO nanoparticles was first well dispersed in 5ml of EA by ultrasonic vibration. Different volume of mixtures were then transferred to reaction cells with different volume of EA and irradiated by an unfocused laser beam (355 nm) for 10 min. During this process, laser melting and fragmentation of LBSO nanoparticles are induced by the

particles' absorption of laser energy resulting in the formation of submicron particles with increased size or nanocrystals with decreased size, as illustrated in **Figure 1e**. When lower laser fluence is used, LBSO submicrometer particles (~300 nm) formed by laser irradiation can be observed from the SEM (**Figure S2**). Once laser energy meets the threshold, raw nanoparticles will tend to be evaporated and nanocrytals can be generated based on the mechanism of photothermal evaporation. As shown in **Figure 1f**, the transmission electron microscopy (TEM) image revealed the generation of monodisperse and uniform-sized colloidal particles with an average size of 2 nm after laser irradiation with fluence of 100 mJ/pulse·cm^2. The interlayer space of about 0.206 nm corresponds to the (200) lattice fringe of BaSnO3, shown as inset in **Figure 1f**, which suggests that the LBSO nanocrystals can be simply generated in EA via a simple laser treatment of LBSO nanoparticles. It should be mentioned that generated transparent colloidal solution emits bright blue emission under UV lamp illumination, and we created a "Sono-laser" logo on the plexiglass substrate by drying the solution (**Figure 1g**) indicating the fluence is originated from the nanocrystals instead of the solvents. We further explored the effect of different laser fluence on nanocrystals and corresponding TEM images (**Figure 1h**) revealed that the size of the nanocrystals can be manipulated via adjusting the laser fluence. LBSO nanocrystals generated under relatively high laser fluence are fairly small (2-3 nm) and well-distributed. Raman spectroscopy (**Figure S3**) also revealed the same peak positions of the nanocrystals indicating a stable crystal structure of LBSO upon pulsed laser irradiation

Perovskite films embedded with LBSO nanocrystals

In comparison to the typical wet chemical synthesis, the monodisperse inorganic nanocrystals with ligand-free feature are generated via the technique of pulsed laser irradiation in liquid, which is specifically favorable for optoelectronic applications. We thus tried to introduce the laser generated LBSO nanocrystals in perovskite films. Deposited with a widely adopted anti-solvent procedure and followed by an annealing treatment (**Figure S4**), $Cs_{0.05}$ $(FA_{0.85}MA_{0.15})_{0.95}PbI_{2.55}Br_{0.45}$ perovskite films employing the generated colloidal solution are denoted as CsFAMA-LBSO (the films using EA as anti-solvent are denoted as CsFAMA). The surface scanning electron microscopes (SEM) images of the two types of perovskite films are shown in **Figures 2a and 2b,** respectively. In contrast to the CsFAMA film, the perovskite film obtained employing the LBSO nanocrystals colloidal solution exhibits smoother surfaces without any residual LBSO nanocrystals aggregates and fewer grain protrusions, which is consistent with the atomic force microscopy (AFM) results (**Figure 2c**). Furthermore, to verify the embedding of LBSO nanocrystals in the perovskite film, cross-section morphologies of perovskite devices are observed by SEM with energy dispersive X-Ray spectroscopy (EDS), as shown in **Figure 1d**. The EDS observation revealed the distribution of Ba elements throughout the perovskite layer (indicated by the Pb and I elements distribution,

detailed mapping information shown in **Figure S5**). Besides, XPS depth profile characterization indicates LBSO nanocrystals can be found both on the surface and interior of the CsFAMA-LBSO film (**Figure S6**). An initial conclusion could be drawn that LBSO nanocrystals are indeed incorporated in the perovskite active layer. The distribution of LBSO nanocrystals was also observed by the cross-sectional backscattered scanning electron (BSE) microscopy and the black dots (low atomic weight of Ba or Sn) separately dispersed throughout the layer of the CsFAMA-LBSO film in contrast to CsFAMA film (**Figure S7**).

The X-ray diffraction (XRD) patterns of perovskite films with and without LBSO nanocrystals embedding showed similar crystallinity and no peak shift can be observed (**Figure S8**), further indicating that the LBSO nanocrystals colloidal solution has no adverse impact on crystallization and phase transformation of perovskite, as well as the fact that LBSO nanocrystals are less likely to enter the perovskite lattice, which is in agreement with the identical absorption onset wavelengths of the perovskite films without and with LBSO embedding (**Figure S9**). We thus speculate that the LBSO nanocrystals most probably distribute at GBs within perovskite films, which is similar with the cases of functional solid additives introduced by dispersing in perovskite precursor [33-35, 37]. To determine the specific location of LBSO nanocrystals, conducting atomic force microscopy (c-AFM) was used to measure the local dark conductivity at grains and GBs. As shown in **Figure 1e**, the dark currents at the GBs were lower than that at the grains for the CsFAMA film indicating a poor conductivity at the GBs. In contrast to the obviously improved conductivity at the GBs for the CsFAMA-LBSO film, we can draw a conclusion that LBSO nanocrystals probably distribute at the GBs of perovskite films [38].

PSCs performance based on the LBSO nanocrystals colloidal solution

To investigate the effects of embedding LBSO nanocrystals on the PSCs performance, we fabricated the planar heterojunction configuration PSC devices of Glass/FTO/TiO$_2$/Perovskite/Spiro-OMeTAD/Au. We employed the LBSO nanocrystals colloidal solutions generated by unfocused laser beam with different fluence (50, 100 and150 mJ/pulse·cm^2) to construct a series of PSCs and explored the appropriate laser irradiation fluence range. It was found that when LBSO nanocrystals colloidal solutions generated at 100 or 150 mJ/pulse·cm^2 were introduced into perovskite films, the devices presented much higher performance especially the J_{sc} and *FF*, as shown in **Figure 3a**, and the parameters of performance are listed in **Table 1**. These results imply the superiority of sub-10 nm nanocrystals on improving PSCs performance.

Furthermore, we incorporated the different concentrations of LBSO nanocrystals colloidal solutions (0.01, 0.05 and 0.2 mg/ml) obtained at 100mJ/pulse·cm^2 for 10 min into the films. As shown in **Figure 3b**, the concentration plays an important role in the performance of PSCs. As the concentration of LBSO nanocrystals increases in EA, the PCE first reaches a peak at 0.05mg/ml. When the concentration is further

increased to 0.2 mg/ml, the poorly dispersed and incompletely irradiated LBSO nanoparticles probably accumulate on the surface of the perovskite film (**Figure S10**), which hinders the carrier transport in the interface between perovskite and Spiro-OMeTAD layer and increases the probabilities of piercing the Spiro-OMeTAD layer that leads to the direct contact between perovskite and Au electrode resulting in obvious deteriorated performance.

To take an overview of the effects of LBSO nanocrystals on PSCs performance, we prepared performance parameters statistics of 15 devices based on the different LBSO nanocrystals colloidal solutions (**Figure 3c-f**). We can observe the significant enhancement in J_{sc} and *FF* while little changed V_{oc} for CsFAMA-LBSO devices under appropriate laser treatment. Comparing with CsFAMA devices, the average PCE of CsFAMA-0.05LBSO devices rises from 19.02% to 20.36%, the average J_{sc} from 22.50 to 23.15 mA/cm^2, as well as the average *FF* from 73.48 % to 76.04 % (**Table 1**). **Figure 3g-h** show the *J-V* curves measured under reverse- and forward-scan directions for CsFAMA and CsFAMA-LBSO perovskite devices with champion PCE. The champion CsFAMA-LBSO device showed a PCE of 21.11% with little hysteresis (**Figure 3h**) and photovoltaic metrics of the device are as follows: short-circuit current (J_{sc}) = 23.78 mA/cm^2 (forward 23.80 mA/cm^2), open-circuit voltage (V_{oc}) = 1.126 V (forward 1.118 V) and FF = 78.88 % (forward 77.52 %). We integrated the external quantum efficiency (EQE) spectra over the AM 1.5G solar spectrum, and the resulting J_{sc} values agreed well with the J_{sc} (deviation <5%) from *J-V* scanning measurement (**Figure 3i**). There is an obviously improved response in the long wavelength range from 600 to 750 nm, indicating more efficient collection of photogenerated electrons than LBSO nanocrystals-free PSC in deep region and accelerating electron extraction and transport due to the embedding of the LBSO nanocrystals in the film of   perovskite[35].

It is worth noting that a champion PCE of 21.11% in the CsFAMA type PSCs based on laser generated LBSO nanocrystals is among the top in the records of the functional solid additives related PSCs performance reported in previous literature, as shown in **Table 2** [33-35, 37, 39-42]. We also tried to disperse an equivalent amount of raw LBSO nanoparticles in the anti-solvent of EA by ultrasonic vibration without laser irradiation. It turns out that this always resulted in nearly unimproved or even deteriorated performance (**Figure S11**) and similar results were also mentioned in the previous research about dispersing GDY in CB as anti-solvent [35], since the raw nanoparticles are most strongly agglomerated (**Figure 1a**) and are easily spun away during a secondary solvent dripping at a high spinning speed of 4000 rpm, which further demonstrate the unique advantage of PLICN technique for generating the monodispersed nanocrystals in the anti-solvents.

In addition, the stability of perovskite devices was investigated, as shown in **Figure S12**. After explosion of nearly 800h with a relative humidity (RH) of 30% at 25°C, the PCE of CsFAMA-LBSO device exhibited 15% dropping in comparison to its initial value while nearly 25% dropping for CsFAMA device. It means that perovskite films with LBSO nanocrystals embedding have slightly stronger resistance to moisture than the control sample, probably due to the improved film quality. Subsequently, we further increased the RH to 70% and all devices showed the accelerated degradation to the same degree (about 15%), but CsFAMA-LBSO device still demonstrated improved stability than that of the control device.

Characterization of perovskite films' electronic property

To further reveal the reason behind the PCE increase of the perovskite film after embedding the LBSO nanocrystals, the steady-state photoluminescence (PL) spectrum of perovskite films was employed to investigate the interaction between perovskite and LBSO nanocrystals. As shown in **Figure 4a**, with the increasing concentration of LBSO nanocrystals, the PL quenching gets stronger indicating the effective extraction of photogenerated carriers at interface of perovskite and LBSO nanocrystals. The time-resolved photoluminescence (TRPL) measurements were used to evaluate the photogenerated carriers lifetimes, as given in **Figure 3b**, revealing a much faster PL decay for the CsFAMA-LBSO perovskite film than that of CsFAMA film. The spectra are fitted by the bi-exponential decay function:

$$Y = A_1 e^{-t/\tau_1} + A_2 e^{-t/\tau_2} \quad (1)$$

including the slow decay related to trap-assisted recombination at defects while fast decay related to bi-molecular recombination of photogenerated free carriers. The average carrier's lifetime (τ_{ave}) was calculated using the equation:

$$\tau_{ave} = \frac{A_1\tau_1 + A_2\tau_2}{A_1 + A_2} \quad (2)$$

where A_1, A_2 are the fitting amplitudes. And the τ_{ave} were 68.51 ns, 35.76 ns and 27.78 ns for CsFAMA, CsFAMA-0.01LBSO and CsFAMA-0.05LBSO films, respectively (detailed fitting parameters presented in **Table S2**). Consistent with the steady state PL results, the dramatically decreased lifetimes indicate that LBSO nanocrystals could help effective charge separation. We also investigated the carriers lifetimes of perovskite films on TiO$_2$ substrates, as shown in **Figure 4c** and τ_{ave} decreased from 32.20 ns to 26.85 ns and 25.48 ns respectively (**Table S3**), suggesting that LBSO nanocrystals existing at GBs could facilitate the electron extraction.

Then we explored the band structures of the LBSO nanocrystals and perovskite via electrochemical cyclic voltammetry (CV) and ultraviolet photoelectron spectroscopy (UPS), respectively. As shown in

Figure 3d, the LUMO level of LBSO nanocrystals estimated from the onset reduction potential is -4.03 eV and the HUMO value is calculated to be -7.05 eV based on the optical bandgap 3.02 eV extracted from Uv-vis spectra (**Figure S13**). Such LUMO level of LBSO nanocrystals is close to that of CsFAMA (-3.97 eV, **Figure S14b**) and is beneficial to electron extraction from perovskite to LBSO nanocrystals, then to TiO$_2$ as well as electron transfer from LBSO nanocrystals to perovskite due to the little barrier (0.06 eV). Based on the above analysis, we present the scenario of the carriers transfer in CsFAMA-LBSO samples as depicted in **Figure 4e**. In brief, the photogenerated carriers are extracted to each electrode due to the appropriate energy level alignment under work condition. However, the trap sites in perovskite films, especially at GBs, result in relative deep trap states level, which would serve as potential well for charge carriers and lead to their serious trapping, accumulation and recombination[43]. When embedding LBSO nanocrystals at GBs, owing to their matched energy level with perovskite matrix and high mobility, they can serve as carrier bridges and electron could transfer more effectively among grains than that of the perovskite films without nanocrystals embedding.

Besides, there is a slight change in the work function of the perovskite film from 4.08 to 4.01 eV when the film is decorated by laser generated LBSO nanocrystals (**Figure S14b**). By taking into account the band gap 1.62 eV extracted from UV-vis spectra for both of perovskite films (**Figure S14a**), the valance band maximum (E_v) and conduction band minimum (E_c), we built energy-level diagrams for the perovskite films (**Figure S14c**) as well as band structure alignment of perovskite devices (**Figure 4f**). In principle, the upper conduction band of CsFAMA-LBSO film than that of CsFAMA film could enhance charge transfer from perovskite to electron transport layer. In addition to energy band alignment, the intrinsic carrier mobility of perovskite films also affects the charge carrier transfer. In order to ascertain the influence of LBSO nanocrystals on electron mobility of perovskite films, the electron-only transportation device was fabricated according to the space-charge limited current (SCLC) model [44]. The dark *J-V* characteristics of the electron-only transportation devices are shown in **Figure 3g**, and corresponding devices model diagram of FTO/TiO$_2$/perovskite/PCBM/Au is shown in the inset. The green line (n=1) corresponds to the Ohmic law, followed by a trap-filled region where current sharply increase and trap-free space charge limit current (SCLC) region, seen as blue lines (n=2). And we can calculate the electron mobility from the following Mott-Gurney law:

$$J = \frac{9}{8}\varepsilon\varepsilon_0\mu\frac{V^2}{L^3} \quad (3)$$

where *J* is the dark current density, ε and ε_0 is the dielectric constants of CsFAMA and the vacuum permittivity, respectively, μ is the carrier mobility, *V* the applied bias voltage and *L* is the thickness of the

8

perovskite film. The calculation results show that the electron mobility of CsFAMA-LBSO devices increases from 7.84×10^{-4} cm^2 / V·s to 5.63×10^{-3} cm^2 / V·s, nearly one order of magnitude, in contrast to the reference devices fabricated using the anti-solvent of EA, which is consistent with faster charge extraction observed from TRPL measurements and could also explain the pronounced enhancement of photo current density. The trap-filled limit voltages (V_{TFL}) are obtained from **Figure 3g** as 0.25 and 0.19 V for CsFAMA and CsFAMA-LBSO films, respectively. The defect density could be calculated by equation [44]

$$N_{defects} = \frac{2\varepsilon\varepsilon_0 V_{TFL}}{eL^2} \quad (4)$$

where e is the elementary charge (1.69×10^{-19} C). Therefore, we estimated the defect densities to be 4.20×10^{15} and 3.19×10^{15} cm^{-3} for CsFAMA and CsFAMA-LBSO films. The slightly decreased defect density for the perovskite film with LBSO nanocrystals embedding is probably due to the improved film quality according to the results from UV-vis spectra and SEM morphology. To investigate the electric property of the interface between LBSO nanocrystals and perovskite and reveal the potential carrier transport behaviors in the PSCs, electrochemical impedance spectroscopy (EIS) measurement was used to study the internal series resistance of PSCs with and without LBSO nanocrystals embedding. The Nyquist plots of these devices were obtained with an applied bias voltage of 1.0V close to the V_{oc} under a 100 mW/cm^2 illumination, as shown in **Figure 3h**. The semicircles located at high-frequency range are the signature of the charge transport resistance (R$_{ct}$). According to the fitting results (**Table S4**), the R$_{ct}$ value of the CsFAMA-LBSO device dramatically decreases from 823.2 Ω to 298.6 Ω as compared to the CsFAMA device, indicating the improved charge transport.

3. Conclusion

In this article we demonstrated the embedding of LBSO nanocrystals in the metal halide perovskite films based on the laser generated colloidal solution containing LBSO nanocrystals in the anti-solvent of EA. Cross-section SEM and c-AFM results confirm the LBSO nanocrystals mainly distribute at GBs of perovskite films. Electron extraction and transport are significantly enhanced due to matched energy level alignment and high electron mobility of LBSO nanocrystals. We consequently achieved improved PSCs performance especially the J_{sc} and FF with the maximum power conversion efficiency (PCE) of up to 21.11% demonstrating prominent superiorities to those devices obtained through anti-solvents. Owing to the ligand-free feature of laser generated nanocrystals, the surface modification deserves to be further investigated in our future work, which is expected to passivate the defects from surface & GBs of polycrystalline perovskite film and achieve further breakthrough of PSCs performance. We believe our

study will provide an effective alternative for intriguing applications in photovoltaics or even beyond optoelectronics based on laser-matter interactions.

4. Experimental Section

Materials: Fluorine-doped tin oxide (FTO) glass substrates (around 1.5 cm×1.5 cm) were obtained from Pilkington and etched by a commercial corporation. Titanium (IV) chloride (TiCl4, 99.6%) was purchased from Alfa Aesar. Anhydrous N, N-dimethylformamide (DMF), dimethyl sulfoxide (DMSO), acetonitrile, ethyl acetate (EA) and Lanthanum(III) nitrate hydrate (La(NO$_3$)$_3$·5H$_2$O, 99%) were purchased from Sigma-Aldrich and were used as received without further purification. CsI (≥99.99%), FAI (≥99.5%), PbI$_2$ (>99.99%), MABr (≥99.5%) and PbBr$_2$ (>99.99%), spiro-OMeTAD (≥99.5%), TBP (>96%), LiTFSI (>99%) and FK209 (>98%) were purchased from Xi'an Polymer Light Technology Corp and used as received. Barium dichloride (BaCl$_2$, ≥99.5%), tin(II) chloride (SnCl$_2$, >98%), hydrogen peroxide aqueous solution (H$_2$O$_2$, 30%), ammonium hydroxide aqueous solution (NH$_4$OH, 25%), and citric acid monohydrate (C$_6$H$_8$O$_7$·H$_2$O, >99.5%) were purchased from Sinopharm Chemical Reagent Co., Ltd. Au particles were obtained from Zhongnuo Advanced Material (Beijing) Co., Ltd. China. Deionized water was used with a resistivity of 18.25 MΩ·cm.

Synthesis of LBSO nanoparticles: LBSO nanoparticles were synthesized following previously reported methods in the literature [16]. In brief, BaCl$_2$·2H$_2$O (0.95 mmol), SnCl$_2$ (1 mmol), C$_6$H$_8$O$_7$·H$_2$O (0.5 mmol) and La (NO$_3$)$_3$·5H$_2$O (0.05 mmol) were dissolved in H$_2$O$_2$ aqueous solution (17mL) using constant stirring. The pH of the reaction solution was adjusted to a value of 10 using ammonia solution with constant stirring, followed by vacuum filtration and sintering at 500 ℃ for 1 h.

Laser generated LBSO nanocrystals synthesis: A Nd: YAG laser (pulse width 10 ns, repetition rate 30 Hz, beam size 10 mm) was used as the laser source for pulsed laser irradiation. To fabricate La:BaSnO$_3$ (LBSO) nanocrystals, 1 mg of as-synthesised LBSO particles were firstly well dispersed in 5 ml of EA (anti-solvent) by ultrasonic vibration. Different volume of mixtures (200μl, 1ml) were then transferred to reaction cells with different volume of EA (3.8 ml, 3 ml), respectively, and irradiated by an unfocused laser beam with a laser fluence of 100 mJ pulse^{-1} cm^{-2} (third harmonic) for 10 min at room temperature.

Substrate Preparation: FTO substrates were cleaned sequentially in Hellmanex detergent, deionized water, acetone and ethanol in an ultrasonic bath, each for 20 min, then dried with a compressed nitrogen gun, and finally treated under an oxygen plasma for 10 min to remove the last traces of organic residues. The compact TiO$_2$ layer was formed through a low temperature synthesis method according to the reported literature. In brief, 900 μl TiCl$_4$ solution was added into 40ml ice water and formed a clear solution. Treated FTO glasses were soaked in the solution at 70°C for 1h and cleaned sequentially in deionized water and ethanol. Finally, the prepared samples were then sintered at 105 °C for 60 min.

Perovskite Solar Cells Fabrication: To generate the mixed perovskite precursor Cs$_{0.05}$FA$_{0.81}$MA$_{0.14}$PbI$_{2.55}$Br$_{0.45}$ with the concentration of 1.3 M, CsI (0.07M), FAI (1.05 M), PbI$_2$ (1.05 M), MABr (0.18 M) and PbBr$_2$ (0.18 M) were stirred in a mixture of DMF and DMSO (4:1 v/v) at 55 °C for 2 h. To prepare perovskite films, 30 μl of perovslite precursor solution was coated onto the FTO/TiO$_2$ substrate in an argon glovebox by a consecutive two-step spin-coating process at 2,000 and 4,000 r.p.m for 10 and 30 s, respectively. During the second step, 200 μl of anti-solvent or anti-colloida-solution was immediately poured on the spinning substrate 10 s prior to the end of the program. Thereafter, the substrate was put onto a hotplate for 60 min at 100 °C, forming the CsFAMA and CsFAMA-LBSO film. After cooling down to room temperature, the hole transport material (HTM) solution was then deposited by spin coating at 6,000 r.p.m. for 30 s. The HTM solution was prepared by dissolving 72.3 mg Spiro-MeOTAD in 1 mL chlorobenzene, in which 28.8 μl of tBP, 17.5 μl of Li-TFSI solution (520 mg/mL in acetonitrile) and 32 μl of FK209 solution (100mg/ml in acetonitrile). The samples were then aged in a desiccator for ~12 hrs. Finally, a 80 nm-thick Au counter electrode was deposited by thermal evaporation.

Device characterization: Simulated AM 1.5G irradiation (100 mW cm^{-2}) was produced by a xenon-lamp-based solar simulator (Oriel 67005, 150 W Solar Simulator) for current density-voltage *(J-V)* measurements. The light intensity was calibrated by a silicon diode (Hamamatsu S1133) equipped with a Schott visible-colour glass filter (KG5 colour-filter). A Keithley 2420 Source-Meter was used for *J-V* measurement. The scanning rate was 0.2 V/s with no device preconditioning, such as light soaking or extended forward voltage biasing in the dark before starting the measurement. External quantum efficiency (EQE) curves were characterized with a Newport QE measurement kit by focusing a monochromatic beam of light onto the devices.

Material characterization: The morphology and structure of the samples were characterized by a field emission SEM with an EDS detector (FEI Nova) and an atomic force microscope (AFM, Bruker Dimension Icon). C-AFM measurements were performed on an Asylum Research MFP-3D-Origin AFM using Au-coated Si conductive probes. X-ray diffraction (XRD) spectra were recorded on a PANAlyticalX'pert

PRO equipped with a diffracted beam monochromator, and a conventional cobalt target X-ray tube set to 40 kV and 30 mA. X-ray photoelectron spectroscopy (XPS) measurements were conducted on an Axis Supra (Kratos). The Valance band (VB) spectra were measured with a monochromatic He I light source (21.22 eV) and a VG Scienta R4000 analyzer. High-resolution transmission electron microscopy (HRTEM) was performed in combination using a FEI Tecnai F30 microscope equipped with a field emission gun (FEG) operated at 300 kV. The absorption was measured using the ultraviolet-visible (UV-vis) spectrophotometer (Perkin-Elmer Lambda 35 UV-vis-NIR). The Raman spectra were obtained using a Renishaw inVia Raman microscope with a 532 nm laser. Electrochemical impedance spectroscopy (EIS) spectra were collected under illumination of AM 1.5G simulated solar light (100 mW cm^{-2}) with the frequency range from 0.1 Hz to 100 kHz.

For the femtosecond laser PL lifetime measurements, the 400 nm pump beam is the frequency doubled output from a 1kHz, 50 fs Coherent LibraTM Regenerative Amplifier (800nm) using a BBO crystal. The emission from the samples is detected by an Optronis OptoscopeTM streak camera system.

Acknowledgement

Reference

[1]   Xing, G.; Mathews, N.; Sun, S.; Lim, S. S.; Lam, Y. M.; Grätzel, M.; Mhaisalkar, S.; Sum, T. C., Long-Range Balanced Electron- and Hole-Transport Lengths in Organic-Inorganic CH3NH3PbI3. *Science* **2013,** *342* (6156), 344-347.

[2]   Kojima, A.; Teshima, K.; Shirai, Y.; Miyasaka, T. Organometal Halide Perovskites as Visible-Light Sensitizers for Photovoltaic Cells. *J. Am. Chem. Soc.* **2009**, *131*, 6050-6051.

[3]   Ball, J. M.; Lee, M. M.; Hey, A.; Snaith, H. J., Low-temperature processed meso-superstructured to thin-film perovskite solar cells. *Energy & environmental science* **2013,** *6* (6), 1739-1743.

[4]   A. Sadhanala, S. Ahmad, B. Zhao, N. Giesbrecht, P. M. Pearce, F. Deschler, R. L. Hoye, K. C. Godel, T. Bein, P. Docampo, S. E. Dutton, M. F. De Volder & R. H. Friend. Blue-green color tunable solution processable organolead chloride-bromide mixed halide perovskites for optoelectronic applications. Nano Lett. 15, 6095-6101 (2015).

[5]   Kojima, A.; Teshima, K.; Shirai, Y.; Miyasaka, T., Organometal Halide Perovskites as Visible-Light Sensitizers for Photovoltaic Cells. *Journal of the American Chemical Society* **2009,** *131* (17), 6050-6051.

[6]   National Center for Photovoltaics (NCPV) at the National Renewable Energy Laboratory (NREL); www.nrel.gov/pv/assets/pdfs/best-research-cell-efficiencies-190416.pdf.

[7]   Pellet, N.; Gao, P.; Gregori, G.; Yang, T. Y.; Nazeeruddin, M. K.; Maier, J.; Gratzel, M., Mixed-organic-cation perovskite photovoltaics for enhanced solar-light harvesting. *Angewandte Chemie* **2014,** *53* (12), 3151-7.

[8]   Jeon, N. J.; Noh, J. H.; Yang, W. S.; Kim, Y. C.; Ryu, S.; Seo, J.; Seok, S. I., Compositional engineering of perovskite materials for high-performance solar cells. *Nature* **2015,** *517*, 476.

[9]   Saliba, M.; Matsui, T.; Seo, J. Y.; Domanski, K.; Correa-Baena, J. P.; Nazeeruddin, M. K.; Zakeeruddin, S. M.; Tress, W.; Abate, A.; Hagfeldt, A.; Gratzel, M., Cesium-containing triple cation perovskite solar cells: improved stability, reproducibility and high efficiency. *Energy & environmental science* **2016,** *9* (6), 1989-1997.

[10]   Burschka, J.; Pellet, N.; Moon, S. J.; Humphry-Baker, R.; Gao, P.; Nazeeruddin, M. K.; Gratzel, M., Sequential deposition as a route to high-performance perovskite-sensitized solar cells. *Nature* **2013,** *499* (7458), 316-9.

[11]   Jeon, N. J.; Noh, J. H.; Kim, Y. C.; Yang, W. S.; Ryu, S.; Seok, S. I., Solvent engineering for high-performance inorganic-organic hybrid perovskite solar cells. *Nature materials* **2014,** *13* (9), 897-903.

[12]   Ke, W.; Xiao, C.; Wang, C.; Saparov, B.; Duan, H. S.; Zhao, D.; Xiao, Z.; Schulz, P.; Harvey, S. P.; Liao, W.; Meng, W.; Yu, Y.; Cimaroli, A. J.; Jiang, C. S.; Zhu, K.; Al-Jassim, M.; Fang, G.; Mitzi, D. B.; Yan, Y., Employing Lead Thiocyanate Additive to Reduce the Hysteresis and Boost the Fill Factor of Planar Perovskite Solar Cells. *Advanced materials* **2016,** *28* (26), 5214-21.

[13]   Niu, T.; Lu, J.; Munir, R.; Li, J.; Barrit, D.; Zhang, X.; Hu, H.; Yang, Z.; Amassian, A.; Zhao, K.; Liu, S. F., Stable High-Performance Perovskite Solar Cells via Grain Boundary Passivation. *Advanced materials* **2018,** *30* (16), e1706576.

[14]   Bi, D.; Li, X.; Milic, J. V.; Kubicki, D. J.; Pellet, N.; Luo, J.; LaGrange, T.; Mettraux, P.; Emsley, L.; Zakeeruddin, S. M.; Gratzel, M., Multifunctional molecular modulators for perovskite solar cells with over 20% efficiency and high operational stability. *Nature communications* **2018,** *9* (1), 4482.

[15]   Heo, J. H.; Im, S. H.; Noh, J. H.; Mandal, T. N.; Lim, C.-S.; Chang, J. A.; Lee, Y. H.; Kim, H.-j.; Sarkar, A.; Nazeeruddin, M. K.; Grätzel, M.; Seok, S. I., Efficient inorganic–organic hybrid heterojunction solar cells containing perovskite compound and polymeric hole conductors. *Nature Photonics* **2013,** *7*, 486.

[16]   Jiang, Q.; Zhang, L.; Wang, H.; Yang, X.; Meng, J.; Liu, H.; Yin, Z.; Wu, J.; Zhang, X.; You, J., Enhanced electron extraction using SnO2 for high-efficiency planar-structure HC(NH2)2PbI3-based perovskite solar cells. *Nature Energy* **2016,** *2*, 16177.

[17]   Arora, N.; Dar, M. I.; Hinderhofer, A.; Pellet, N.; Schreiber, F.; Zakeeruddin, S. M.; Grätzel, M., Perovskite solar cells with CuSCN hole extraction layers yield stabilized efficiencies greater than 20%. *Science* **2017,** *358* (6364), 768-771.

[18]   Shin, S. S.; Yeom, E. J.; Yang, W. S.; Hur, S.; Kim, M. G.; Im, J.; Seo, J.; Noh, J. H.; Seok, S. I., Colloidally prepared La-doped BaSnO3 electrodes for efficient, photostable perovskite solar cells. *Science* **2017,** *356* (6334), 167-171.

[19]   M. Xiao, F. Huang, W. Huang, Y. Dkhissi, Y. Zhu, J. Etheridge, A. Gray-Weale, U. Bach, Y. B. Cheng & L. Spiccia. A fast

deposition-crystallization procedure for highly efficient lead iodide perovskite thin-film solar cells. *Angew. Chem. Int. Ed.* **126**, 10056-10061 (2014).

[20]   N. Ahn, D.-Y. Son, I.-H. Jang, S.M. Kang, M. Choi & N.-G. Park. Highly reproducible perovskite solar cells with average efficiency of 18.3% and best efficiency of 19.7% fabricated via lewis base adduct of lead(II) iodide. *J. Am. Chem. Soc.* **137**, 8696-8699 (2015).

[21]   T. Bu, L. Wu, X. Liu, X. Yang, P. Zhou, X. Yu, T. Qin, J. Shi, S. Wang, S. Li, Z. Ku, Y. Peng, F. Huang, Q. Meng, Y.-B. Cheng & J. Zhong. Synergic interface optimization with green solvent engineering in mixed perovskite solar cells. *Adv. Energy Mater.* **7**, 1700576 (2017).

[22]   Y. Wang, J. Wu, P. Zhang, D. Liu, T. Zhang, L. Jia, X. Gua, Z. D. Chen & S. Li. Stitching triple cation perovskite by a mixed anti-solvent process for high performance perovskite solar cells   *Nano Energy* **39**, 616-625 (2017).

[23]   Y. Yu, S. Yang, L. Lei, Q. Cao, J. Shao, S. Zhang & Y. Liu. Ultrasmooth perovskite film via mixed anti-solvent strategy with improved Efficiency. *ACS Appl. Mater. Interfaces* **9**, 3667-3676 (2017) .

[24]   Ngo, T. T.; Suarez, I.; Antonicelli, G.; Cortizo-Lacalle, D.; Martinez-Pastor, J. P.; Mateo-Alonso, A.; Mora-Sero, I., Enhancement of the Performance of Perovskite Solar Cells, LEDs, and Optical Amplifiers by Anti-Solvent Additive Deposition. *Advanced materials* **2017**, *29* (7).

[25]   Bi, D.; Yi, C.; Luo, J.; Décoppet, J.-D.; Zhang, F.; Zakeeruddin, Shaik M.; Li, X.; Hagfeldt, A.; Grätzel, M., Polymer-templated nucleation and crystal growth of perovskite films for solar cells with efficiency greater than 21%. *Nature Energy* **2016**, *1*, 16142.

[26]   Niu, T.; Lu, J.; Munir, R.; Li, J.; Barrit, D.; Zhang, X.; Hu, H.; Yang, Z.; Amassian, A.; Zhao, K.; Liu, S. F., Stable High-Performance Perovskite Solar Cells via Grain Boundary Passivation. *Advanced materials* **2018**, *30* (16), e1706576.

[27]   Guo, P.; Ye, Q.; Yang, X.; Zhang, J.; Xu, F.; Shchukin, D.; Wei, B.; Wang, H., Surface & grain boundary co-passivation by fluorocarbon based bifunctional molecules for perovskite solar cells with efficiency over 21%. *Journal of Materials Chemistry A* **2019**, *7* (6), 2497-2506.

[28]   Yang, J.; Ling, T.; Wu, W.-T.; Liu, H.; Gao, M.-R.; Ling, C.; Li, L.; Du, X.-W., A top–down strategy towards monodisperse colloidal lead sulphide quantum dots. *Nature communications* **2013,** *4*, 1695.

[29]   Zeng, H.; Yang, S.; Cai, W., Reshaping Formation and Luminescence Evolution of ZnO Quantum Dots by Laser-Induced Fragmentation in Liquid. *The Journal of Physical Chemistry C* **2011,** *115* (12), 5038-5043.

[30]   Singh, S. C., Mishra, S. K., Srivastava, R. K. & Gopal, R. Optical properties of selenium quantum dots produced with laser irradiation of water suspended Sc nanoparticles. J. Phys. Chem. C 114, 17374–17384 (2010).

[31]   Zhu, L.; Shao, Z.; Ye, J.; Zhang, X.; Pan, X.; Dai, S., Mesoporous BaSnO3 layer based perovskite solar cells. *Chemical communications* **2016,** *52* (5), 970-3.

[32]   Shin, S. S.; Suk, J. H.; Kang, B. J.; Yin, W.; Lee, S. J.; Noh, J. H.; Ahn, T. K.; Rotermund, F.; Cho, I. S.; Seok, S. I., Energy-level engineering of the electron transporting layer for improving open-circuit voltage in dye and perovskite-based solar cells. *Energy & environmental science* **2019,** *12* (3), 958-964.

[33]   Wang, K.; Liu, C.; Du, P.; Zheng, J.; Gong, X., Bulk heterojunction perovskite hybrid solar cells with large fill factor. *Energy & environmental science* **2015,** *8* (4), 1245-1255.

[34]   Chiang, C.-H.; Wu, C.-G., Bulk heterojunction perovskite–PCBM solar cells with high fill factor. *Nature Photonics* **2016,** *10*, 196.

[35]   Li, H.; Zhang, R.; Li, Y.; Li, Y.; Liu, H.; Shi, J.; Zhang, H.; Wu, H.; Luo, Y.; Li, D.; Li, Y.; Meng, Q., Graphdiyne-Based Bulk Heterojunction for Efficient and Moisture-Stable Planar Perovskite Solar Cells. *Advanced Energy Materials* **2018,** *8* (30), 1802012.

[36]   James Allen, S.; Raghavan, S.; Schumann, T.; Law, K.-M.; Stemmer, S., Conduction band edge effective mass of La-doped BaSnO3. *Applied Physics Letters* **2016,** *108* (25), 252107.

[37]   Ma, Y.; Zhang, H.; Zhang, Y.; Hu, R.; Jiang, M.; Zhang, R.; Lv, H.; Tian, J.; Chu, L.; Zhang, J.; Xue, Q.; Yip, H.-L.; Xia, R.; Li, X. a.; Huang, W., Enhancing the Performance of Inverted Perovskite Solar Cells via Grain Boundary Passivation with Carbon Quantum Dots. *ACS applied materials & interfaces* **2019,** *11* (3), 3044-3052.

[38]   Wu, Q. Wang, Y. Fang, Y. Shao, S. Tang, Y. Deng, H. Lu, Y. Liu, T. Li, Z. Yang, A. Gruverman & J. Huang. Molecular doping enabled scalable blading of efficient hole-transport-layer-free perovskite solar cells. *Nat. Commun.* **9**, 1625 (2018).

[39]   Tong, T. T.; Li, X. H.; Guo, S. H.; Han, J.; Wei, B. Q., Sequential solvent processing with hole transport materials for improving efficiency of traditionally-structured perovskite solar cells. *Nano Energy* **2017,** *41*, 591-599.

[40]   Gao, Y.; Wu, Y.; Lu, H.; Chen, C.; Liu, Y.; Bai, X.; Yang, L.; Yu, W. W.; Dai, Q.; Zhang, Y., CsPbBr3 perovskite nanoparticles as additive for environmentally stable perovskite solar cells with 20.46% efficiency. *Nano Energy* **2019,** *59*, 517-526.

[41]   Zheng, X.; Troughton, J.; Gasparini, N.; Lin, Y.; Wei, M.; Hou, Y.; Liu, J.; Song, K.; Chen, Z.; Yang, C.; Turedi, B.; Alsalloum, A. Y.; Pan, J.; Chen, J.; Zhumekenov, A. A.; Anthopoulos, T. D.; Han, Y.; Baran, D.; Mohammed, O. F.; Sargent, E. H.; Bakr, O. M., Quantum Dots Supply Bulk- and Surface-Passivation Agents for Efficient and Stable Perovskite Solar Cells. *Joule* **2019**.

[42]   Guo, P.; Yang, X.; Ye, Q.; Zhang, J.; Wang, H.; Yu, H.; Zhao, W.; Liu, C.; Yang, H.; Wang, H., Anti-Colloidal-Solutions: Laser-Generated Nanocrystals in Perovskite: Universal Embedding of Ligand-Free and Sub-10 nm Nanocrystals in Solution-Processed Metal Halide Perovskite Films for Effectively Modulated Optoelectronic Performance. *Advanced Energy Materials* **2019**, *9*, 1970134.

[43]   Ye, S.; Rao, H.; Zhao, Z.; Zhang, L.; Bao, H.; Sun, W.; Li, Y.; Gu, F.; Wang, J.; Liu, Z.; Bian, Z.; Huang, C., A Breakthrough Efficiency of 19.9% Obtained in Inverted Perovskite Solar Cells by Using an Efficient Trap State Passivator Cu(thiourea)I. *Journal of the American Chemical Society* **2017**, 139, 7504-7512.

[44]   Dong, Q.; Fang, Y.; Shao, Y.; Mulligan, P.; Qiu, J.; Cao, L.; Huang, J., Electron-hole diffusion lengths > 175 μm in solution-grown CH3NH3PbI3 single crystals. *Science* **2015**, *347* (6225), 967-970.
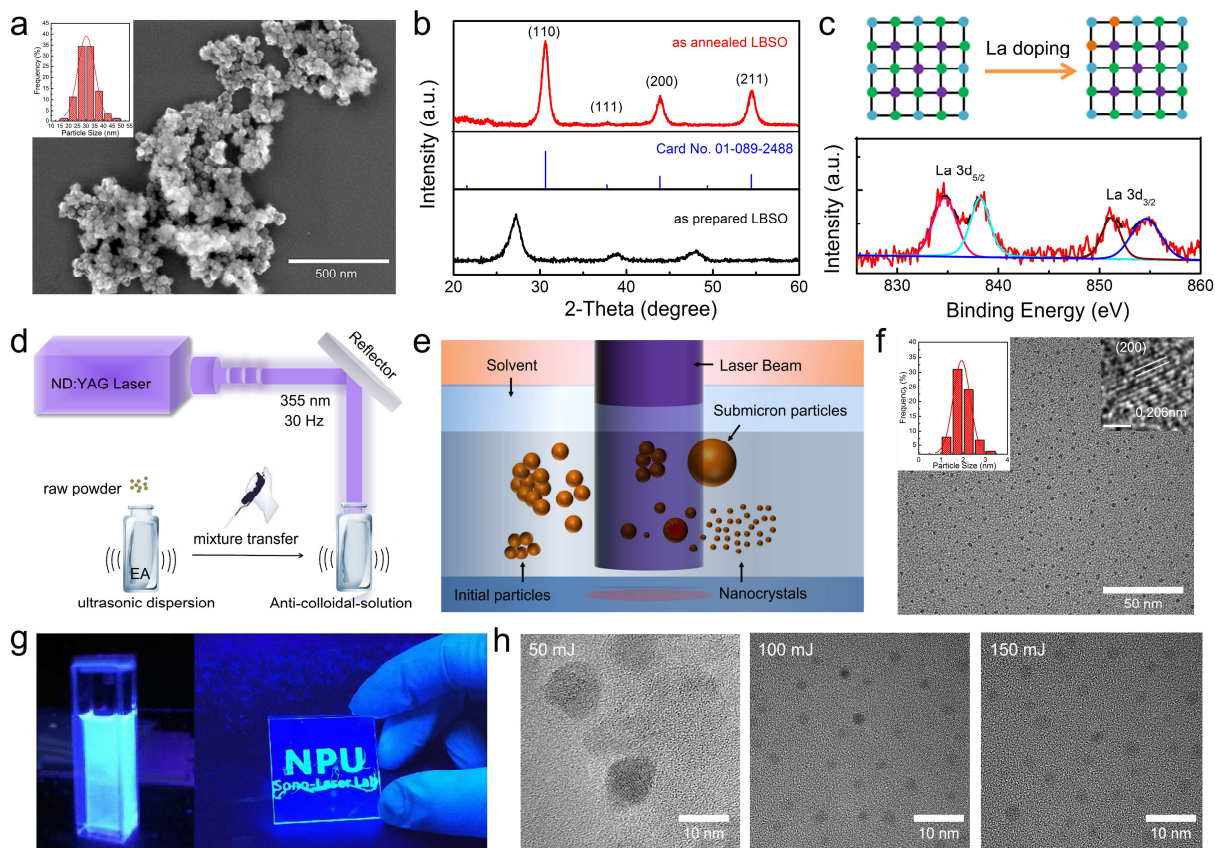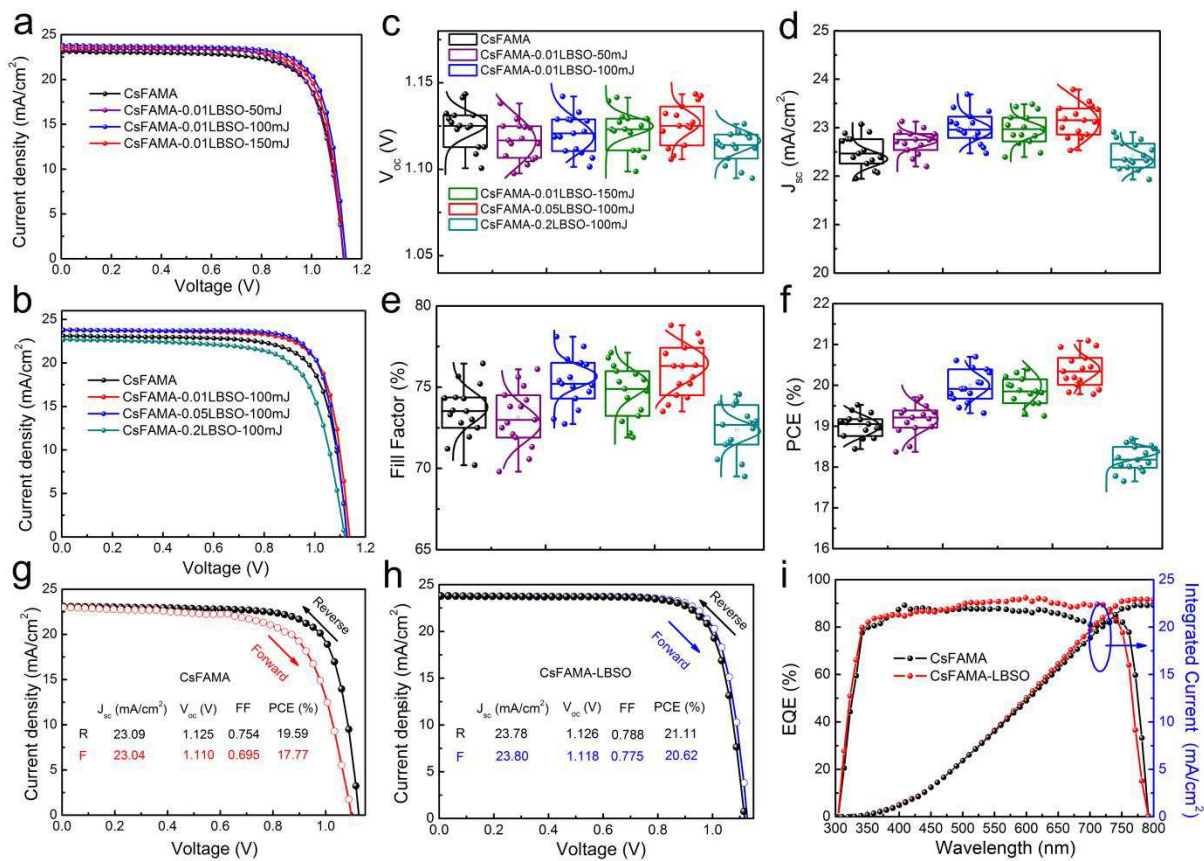
Figure 1 LBSO nanocrystals generated by pulsed laser irradiation. (a) SEM observation of raw LBSO nanoparticles and size distribution (inset). **(b)** XRD pattern of raw LBSO nanoparticles synthesized following the two-step reaction. **(c)** Schematic diagram of La atom doping (orange, green, blue, and purple dots represent the La, Ba, Sn and O atom of the LBSO lattice, respectively) and binding energy spectrum of La. **(d)** Schematic illustration of the preparation of LBSO nanocrystals in anti-solvent of EA. **(e)** Schematic illustration of pulsed laser irradiation. **(f)** TEM image of monodisperse colloidal particles generated by pulsed laser irradiation, size distribution and HR-TEM image of LBSO nanocrystals (inset). **(g)** Image of colloidal solution and "logo" created by colloidal solution under UV lamp illumination. **(h)** TEM images of LBSO nanocrystals generated under different laser energy.
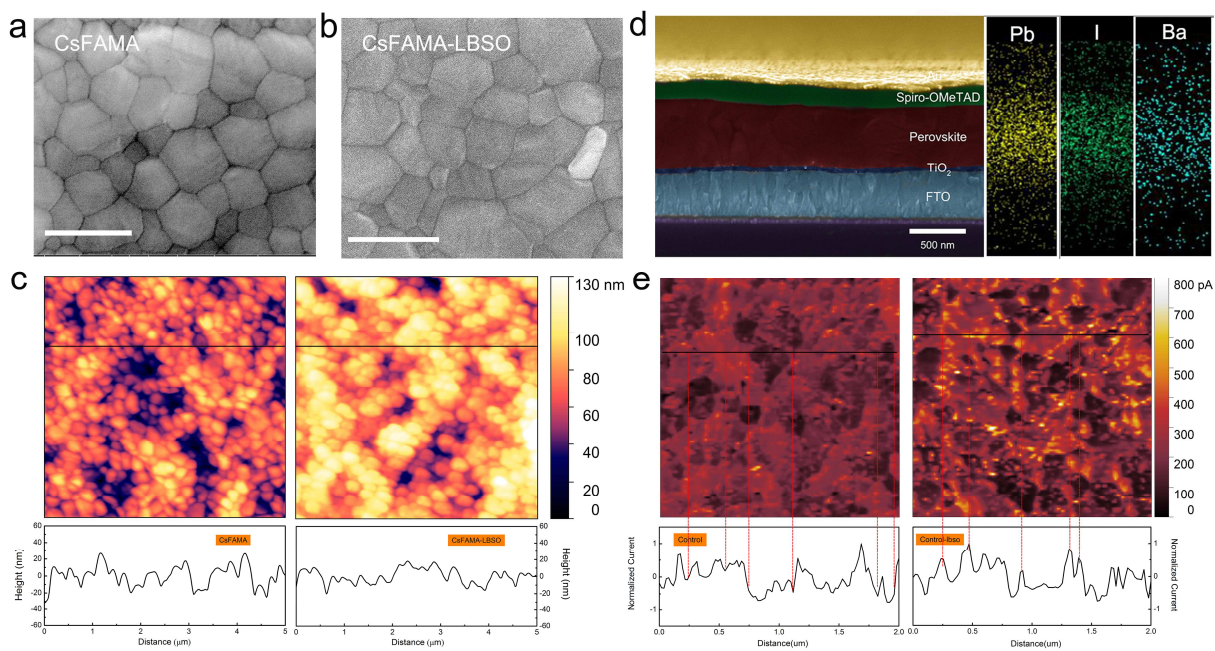
Figure 2 Perovskite films embedded with LBSO nanocrystals. SEM images of the CsFAMA **(a)** and CsFAMA-LBSO **(b)** perovskite films. The scale bar is 500 nm. **(c)** AFM images of CsFAMA (left) and CsFAMA-LBSO (right) films, the corresponding height curves were extracted from black line cut, respectively. **(d)** Cross-section SEM image and corresponding SEM-EDS mappings (Pb, I and Ba) of the CsFAMA-LBSO device. **(e)** c-AFM images of CsFAMA (left) and CsFAMA-LBSO (right) films, the corresponding current curves were extracted from black line cut, respectively.

Figure 3 PSCs performance based on LBSO nanocrystals colloidal solution. (a) J-V curves of the champion cells based on the 0.01mg/ml LBSO nanocrystals anti-colloidal-solution generated by unfocused laser beam with different fluence. **(b)** J-V curves of the champion cells based on the different concentrations of LBSO anti-colloidal-solution generated by unfocused laser beam with 100 mJ/pulse·cm^2 fluence. Statistics of performance parameters **(c)** V_{oc}, **(d)** J_{sc}, **(e)** *FF* and **(f)** *PCE* for PSCs fabricated by various anti-colloidal-solutions generated at different laser irradiation experimental conditions. *J-V* curves measured by reverse and forward scans of the champion cells for CsFAMA **(g)** and CsFAMA-LBSO **(h)**. **(e)** EQE and integrated current density curves of the champion devices for CsFAMA and CsFAMA-LBSO.

17
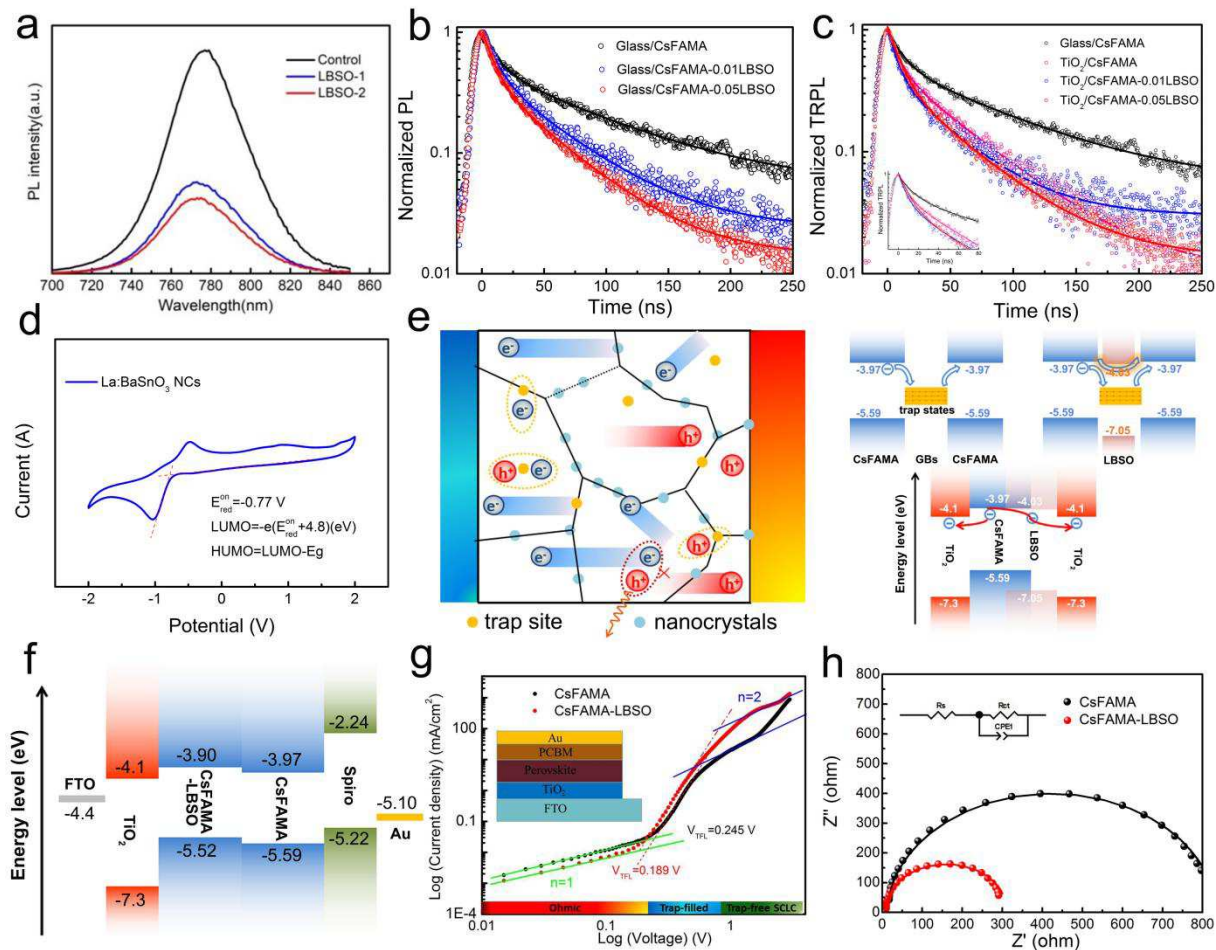
Figure 4 Photoelectric property characterizations of perovskite films. (**a**) Steady-state PL spectra and (**b, c**) TRPL spectra of CsFAMA and CsFAMA-LBSO films. (**d**) Cyclic voltammetry scans for LBSO nanocrystals. (**e**) Illumination of carrier movement process. (**f**) Energy level alignment in perovskite devices. (**g**) Dark J-V curves of electron-only perovskite devices. (**h**) Nyquist plots of perovskite devices measured at 1.0 V bias and under illumination of 100 mW/cm^2.

Table 1 Photovoltaic parameters for devices fabricated by various colloidal solutions generated at different laser irradiation conditions.

Device	J_{sc} (mA/cm^2)	V_{oc} (V)	FF (%)	PCE (%)	PCE$_{BEST}$ (%)
CsFAMA	22.50 ± 0.34	1.124 ± 0.012	73.48 ± 1.66	19.02 ± 0.29	19.59
CsFAMA-0.01LBSO-50mJ	22.70 ± 0.25	1.118 ± 0.010	73.13 ± 1.82	19.16 ± 0.38	19.78
CsFAMA-0.01LBSO-100mJ	23.01 ± 0.33	1.120 ± 0.013	75.32 ± 1.55	20.00 ± 0.42	20.70
CsFAMA-0.01LBSO-150mJ	22.96 ± 0.33	1.121 ± 0.011	74.70 ± 1.64	19.85 ± 0.34	20.36
CsFAMA-0.05LBSO-100mJ	23.15 ± 0.34	1.125 ± 0.013	76.04 ± 1.62	20.36 ± 0.42	21.11
CsFAMA-0.2LBSO-100mJ	22.43 ± 0.28	1.112 ± 0.009	72.38 ± 1.52	18.20 ± 0.31	18.69

* Reverse scans were measured for all devices and 15 cells were fabricated for each type of devices.

Table 2 Summary of functional solid additives related to PSCs performance improvement collected from the most-recent literature

Solid additives	Average PCE before treatment (%)	Average PCE after treatment (%)	Champion PCE (%)	Perovskite type	Introducing methods	Ref.
$A_{10}C_{60}$		13.97	11.45/14.34	MAPbI$_3$	Precursor	33
PCBM			11.40/16.00	MAPbI$_3$	Precursor	34
GDY	19.61	20.12	20.06/20.55	FA$_{0.85}$MA$_{0.15}$Pb(I$_{0.85}$Br$_{0.15}$)$_3$	Precursor	35
CDs	~15	~17.5	15.67/18.24	MAPbI$_3$	Precursor	37
Spiro-OMeTAD			15.00/18.39	MAPbI$_3$	Anti-solvent	39
CsPbBr$_3$ QDs	~18	20	18.51/20.46	MAPbI$_3$	Anti-solvent	40
CsPbBrCl$_2$ QDs	~18.5	~20.5	~20.5/21.5	MAPbI$_3$	Anti-solvent	41
Cl-CDs	19.04	20.78	19.59/21.39	Cs$_{0.05}$FA$_{0.81}$MA$_{0.14}$PbI$_{2.55}$Br$_{0.45}$	Anti-solvent	42
La:BaSnO$_3$ nanocrystals	19.02	20.36	19.59/21.11	Cs$_{0.05}$FA$_{0.81}$MA$_{0.14}$PbI$_{2.55}$Br$_{0.45}$	Anti-solvent	Our work

Supplemental Materials

Boosted Carriers Extraction and Transport in Solution Processed Perovskite Film Decorated by Laser Generated La-doped BaSnO₃ Nanocrystals

Xiaokun Yang [a, b], Linfeng Ye [a], Pengfei Guo [a], Youxun Xu [a], Hang Guo[a], Qian Ye [a], Hongyue Wang [a], Huiwu Yu [a], Tze-Chien Sum[b], Dmitry Shchukin* [c], [d], Hongqiang Wang* [a]

[a]*State Key Laboratory of Solidification Processing, Center for Nano Energy Materials, School of Materials Science and Engineering, Northwestern Polytechnical University and Shaanxi Joint Laboratory of Graphene (NPU), Xi'an, 710072, P. R. China*

Email: hongqiang.wang@nwpu.edu.cn

[b]*School of Physical & Mathematical Sciences, Nanyang Technological University, 21 Nanyang Link, Singapore 637371*

[c]*Stephenson Institute for Renewable Energy, Department of Chemistry, University of Liverpool, Crown Street, Liverpool, L69 7ZD, UK*

Email: d.shchukin@liverpool.ac.uk

[d]*Gubkin University, 19991, Russia, Moscow, 65/1 Leninsky prospect.*

Key words: ternary metal oxide; metal halide perovskite films; laser generated nanocrystals
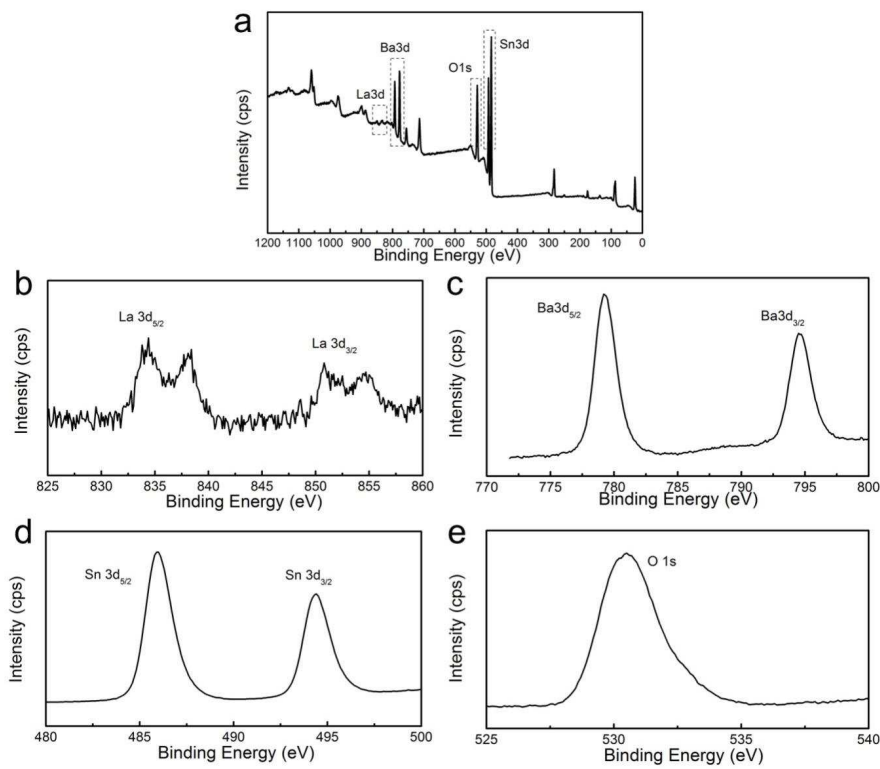
Figure S1 (a) XPS spectrum and binding energies of **(b)** La3d, **(c)** Ba3d, **(d)** Sn3d, and **(d)** O1s of the synthesized LBSO nanoparticles.
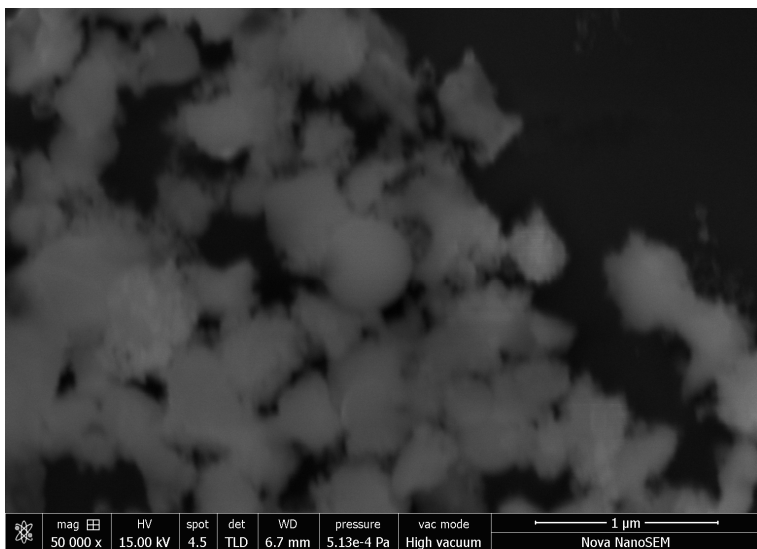
Figure S2 SEM image of LBSO submicron particles formed by laser irradiation with a fluence of 30mJ/pulse cm^2.
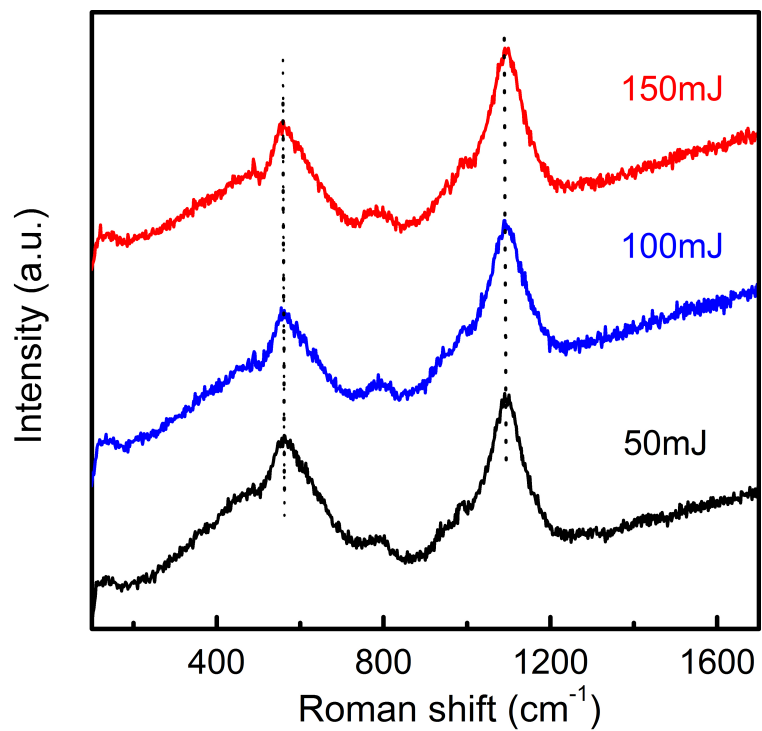
Figure S3 Roman spectra of LBSO nanocrystals generated under different laser energy (50, 100 and 150 mJ/pulse·cm^2).
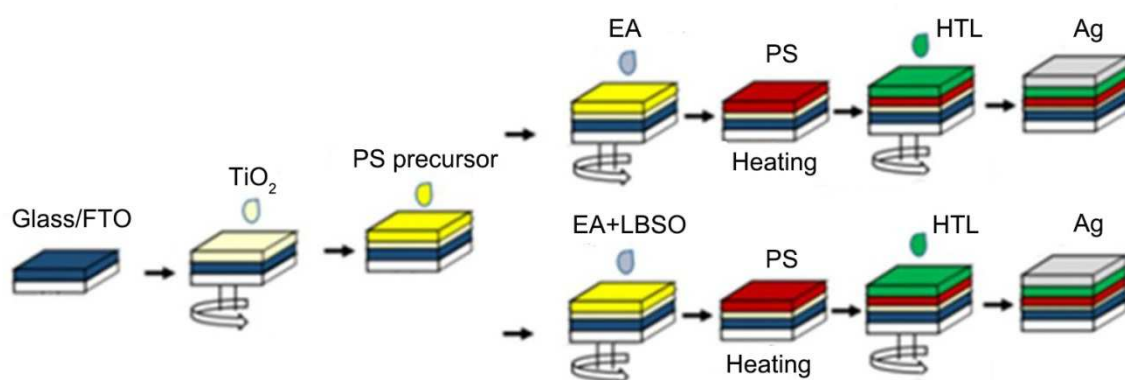
Figure S4 Schematic illustration of the fabrication procedures for the Perovskite solar cells via anti-solvent of EA and anti-colloidal-solution deposition.
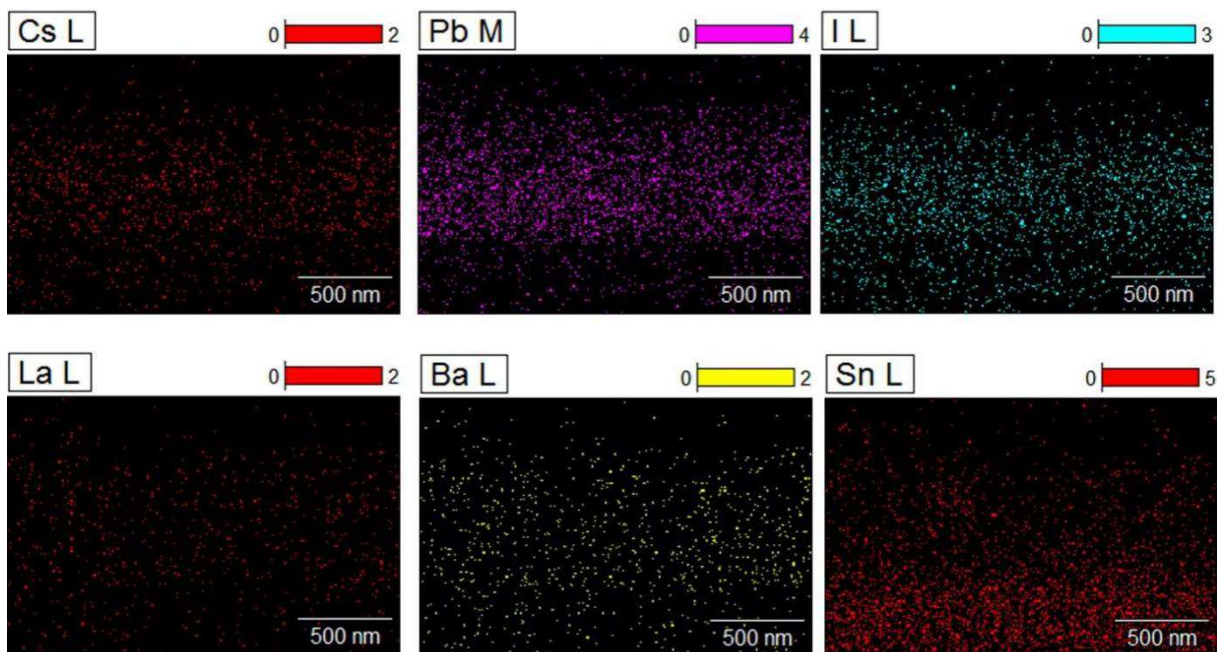
Figure S5 EDS mapping of Cs, Pb, I, La, Ba and Sn for CsFAMA-LBSO film.
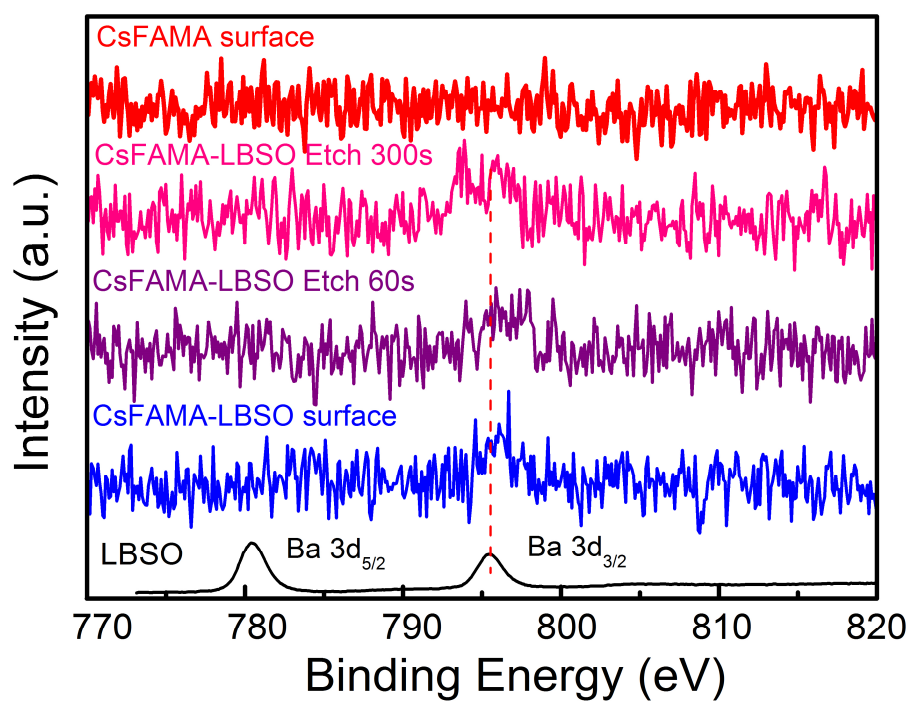
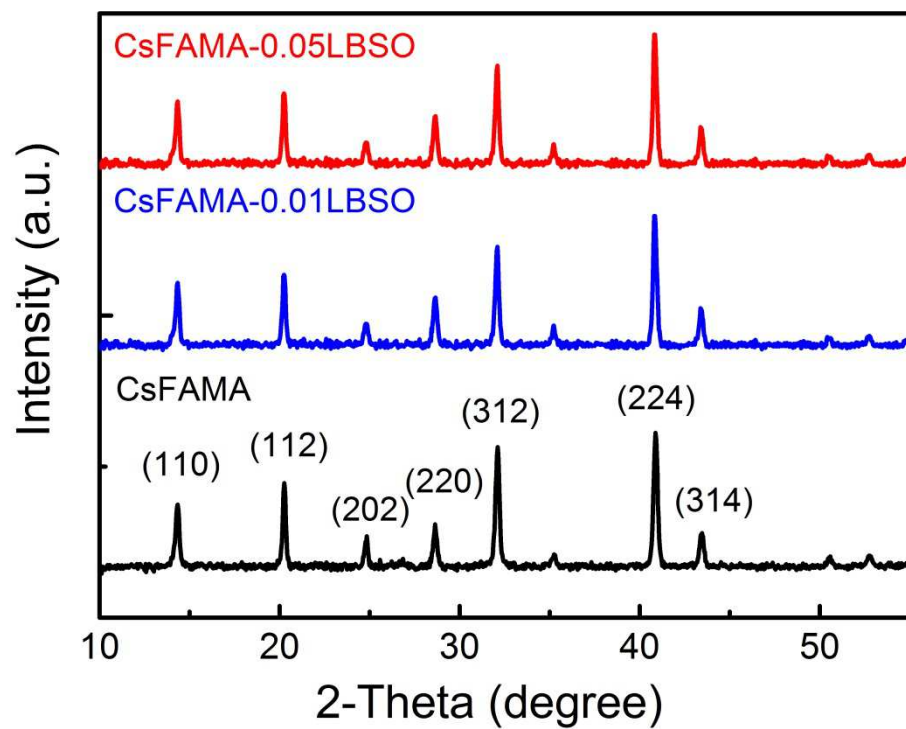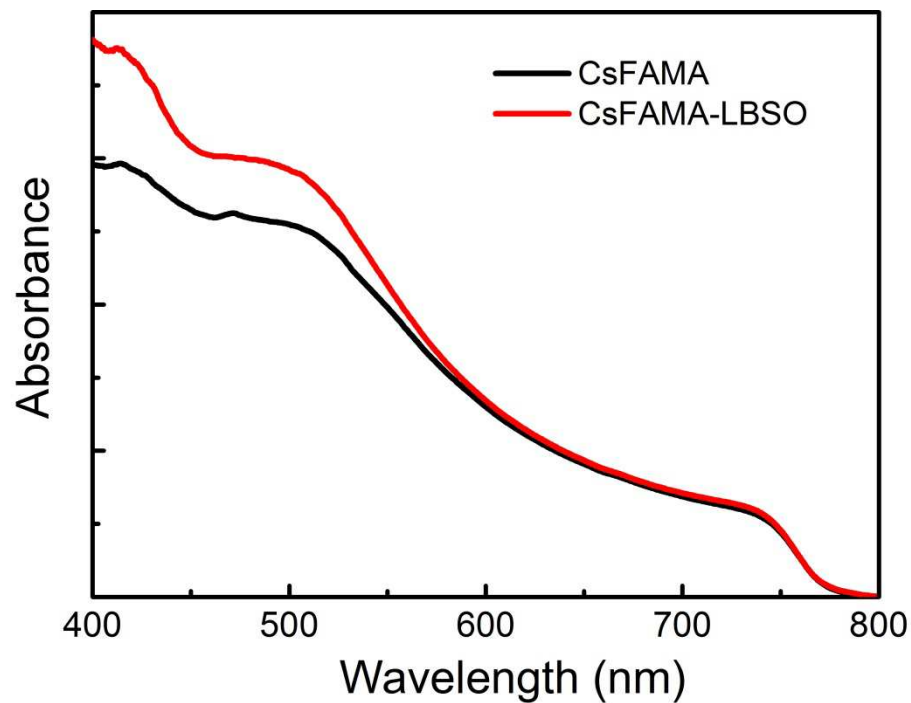**Figure S6** XPS spectrum of Ba 3d peaks of CsFAMA-LBSO and CsFAMA film.
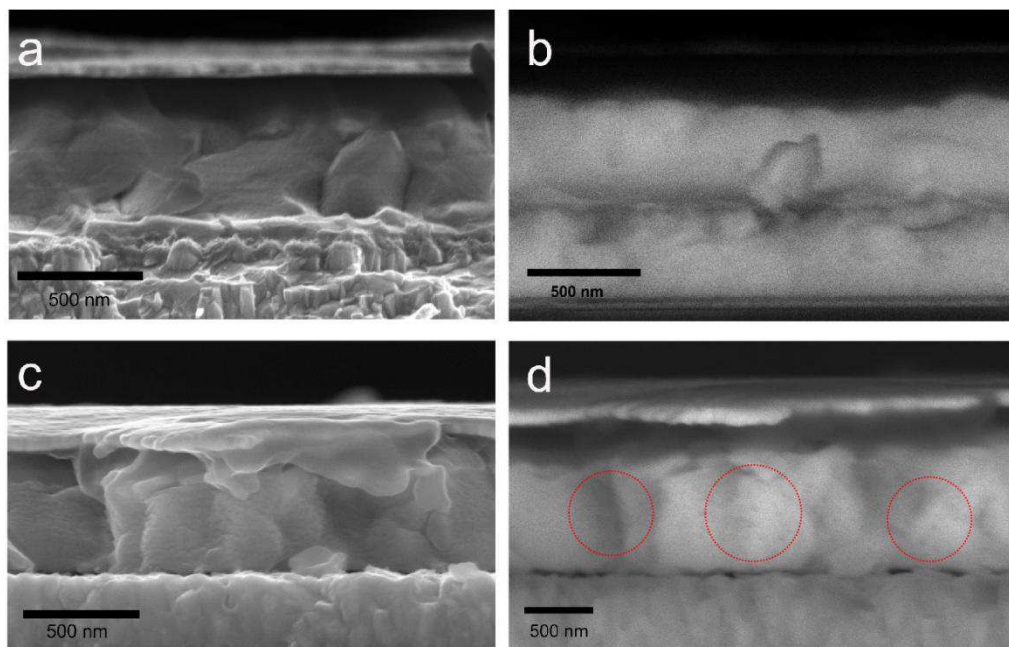
Figure S7 Cross-sectional second electron (SE) and backscattered electron (BSE) images of CsFAMA **(a, b)** and CsFAMA-LBSO **(c, d)**.

Figure S8 XRD patterns of the different perovskite films: CsFAMA, CsFAMA-0.01LBSO and CsFAMA-0.05LBSO.

Figure S9 Uv-vis spectra of the different perovskite films: CsFAMA and CsFAMA-LBSO.

Table S1 Summary of the champion performance for devices fabricated by various anti-colloidal-solutions generated at different experimental conditions.

Devices	J_{sc} (mA cm^{-2})	V_{oc} (V)	FF (%)	Efficiency (%)
CsFAMA	23.09	1.125	75.40	19.59
CsFAMA-0.01LBSO-50mJ	23.29	1.127	75.35	19.78
CsFAMA-0.01LBSO-100mJ	23.69	1.134	77.06	20.70
CsFAMA-0.01LBSO-150mJ	23.55	1.127	76.69	20.36
CsFAMA-0.05LBSO-100mJ	23.78	1.126	78.82	21.11
CsFAMA-0.2LBSO-100mJ	22.81	1.117	73.48	18.72
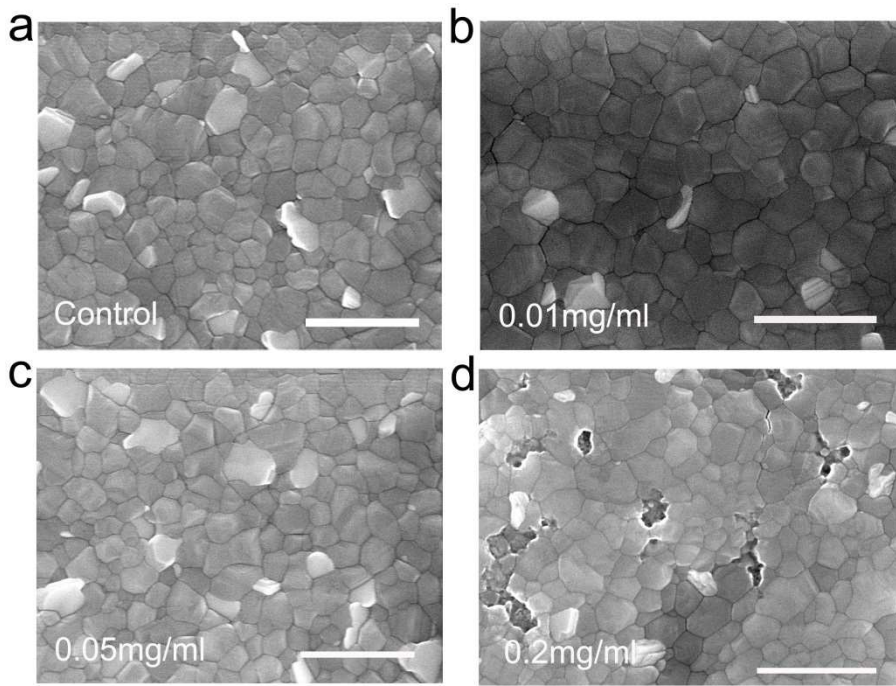
Figure S10 Surface morphologies of the perovskite films prepared by employing different concentrations of LBSO nanocrystals colloidal solutions: **(a)** CsFAMA, **(b)** 0.01mg/ml, **(c)** 0.05mg/ml, and **(d)** 0.2mg/ml. The scale bar is 1 μm.
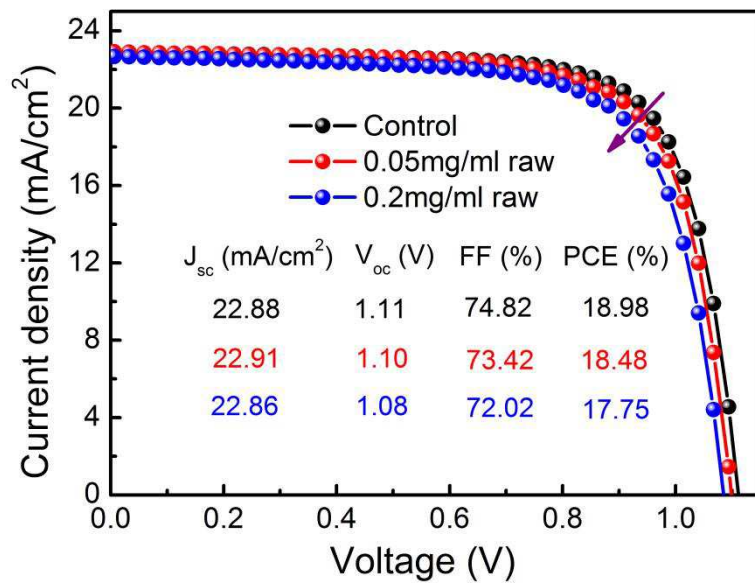
Figure S11 *J-V* curves of the cells for CsFAMA and CsFAMA-raw LBSO at different concentrations (0.01, 0.05 and 0.2 mg/ml)
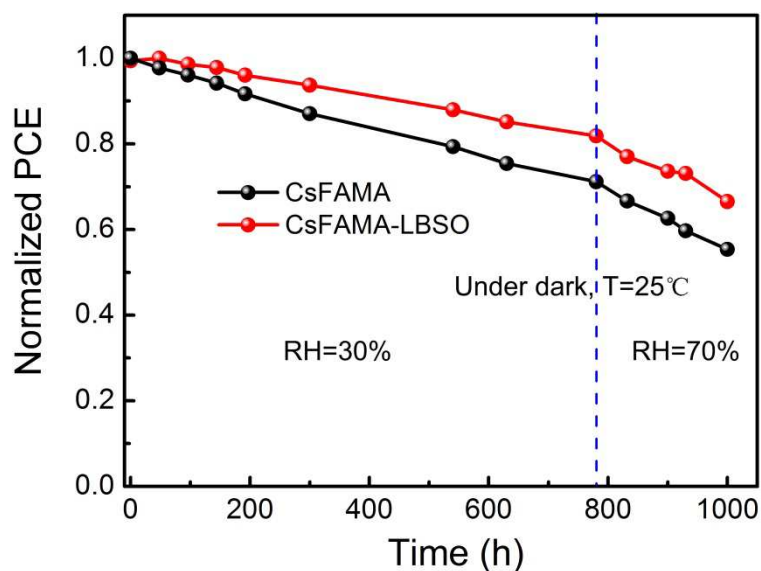
Figure S12 Humidity stability test for unencapsulated CsFAMA and CsFAMA-LBSO devices. The devices are kept successively in two constant temperature & humidity incubators (relative humidity: 30% and 70% respectively) in dark and measured regularly in air.

Table S2 Summary of fitting parameters of TRPL for different perovskite film deposited on Glass substrates.

Sample	A_1	τ_1 (ns)	A_2	τ_2 (ns)	τ_{ave} (ns)
CsFAMA	0.43	137.85 ± 1.21	0.57	16.20 ± 0.25	68.51
CsFAMA-0.01LBSO	0.30	86.27 ± 1.54	0.70	14.11 ± 0.24	35.76
CsFAMA-0.05LBSO	0.35	59.99 ± 0.59	0.65	10.43 ± 0.13	27.78

Table S3 Summary of fitting parameters of TRPL for different perovskite film deposited on Glass/FTO/TiO$_2$ substrates.

Sample	A_1	τ_1 (ns)	A_2	τ_2 (ns)	τ_{ave} (ns)
CsFAMA	0.45	59.82 ± 0.52	0.55	9.30 ± 0.17	32.20
CsFAMA-0.01LBSO	0.29	65.77 ± 0.70	0.71	10.96 ± 0.12	26.85
CsFAMA-0.05LBSO	0.34	56.96 ± 4.70	0.66	9.26 ± 0.35	25.48
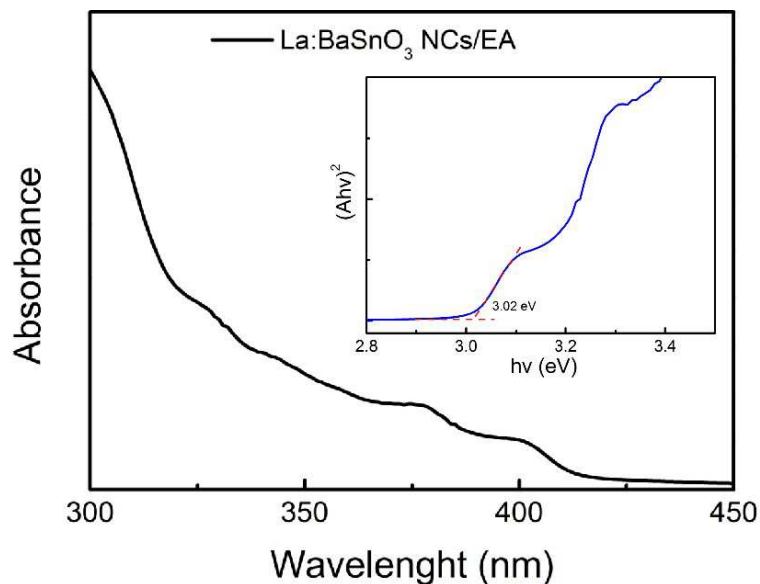
Figure S13 Uv-vis spectra of LBSO nanocrystals colloidal solution and corresponding $(ahv)^2$ versus hv plots.
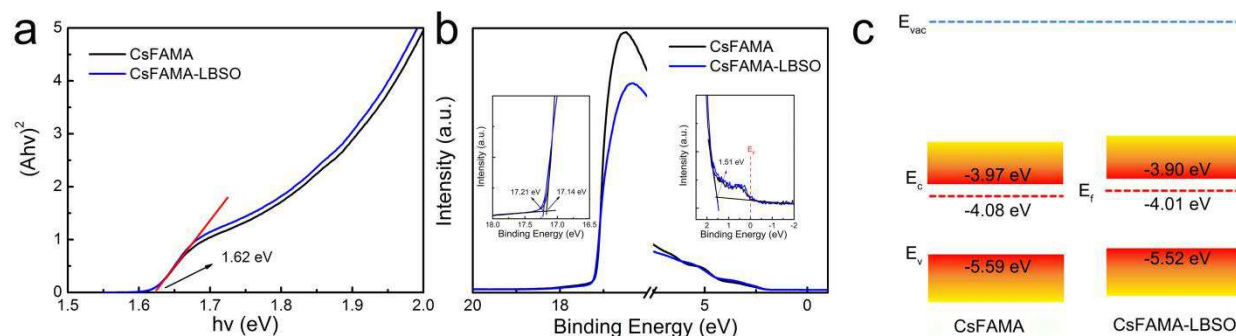
Figure S14 (a) $(ahv)^2$ versus hv plots of perovskite films. **(b)** UPS measurements of perovskite films, the insets are the amplification for binding energy from 18.0 to 16.5 eV and 2.5 to -2.0 eV, respectively. **(c)** Schematic energy level diagrams of CsFAMA and CsFAMA-LBSO films.

Table S4 Summary of fitting parameters of Nyquist plots for different perovskite cells.

Sample	Rs (Ω)	Rct (Ω)	CPE-T (F)	CPE-P
CsFAMA	11.52	823.2	4.577×10^{-9}	0.9802
CsFAMA-LBSO	10.8	298.6	4.344×10^{-9}	1.051